The x-ray light valve: A low-cost, digital radiographic imaging system—Spatial resolution

Robert D. MacDougall, Ivaylo Koprinarov, and J. A. Rowlands[a)]
Imaging Research, Sunnybrook Health Sciences Centre, Department of Medical Biophysics, University of Toronto, 2075 Bayview Avenue, Toronto, Ontario M4N 3M5, Canada

(Received 16 January 2008; revised 14 July 2008; accepted for publication 16 July 2008; published 25 August 2008)

An x-ray light valve (XLV) coupled with an optical scanner has the potential to meet the need for a low-cost, high quality digital imaging system for general radiography. The XLV/scanner concept combines three well-established, and hence, low-cost technologies: An amorphous selenium (*a*-Se) layer as an x-ray-to-charge transducer, a liquid crystal (LC) cell as an analog display, and an optical scanner for image digitization. The XLV consists of an *a*-Se layer and LC cell in a sandwich structure which produces an optical image in the LC layer upon x-ray exposure. The XLV/scanner system consists of an XLV in combination with an optical scanner for image readout. Here, the effect of each component on the spatial resolution of an XLV/scanner system is investigated. A theoretical model of spatial resolution of an XLV is presented based on calculations of the modulation transfer function (MTF) for *a*-Se and a LC cell. From these component MTFs, the theoretical MTF of the XLV is derived. The model was validated by experiments on a prototype XLV/scanner system. The MTF of the scanner alone was obtained by scanning an optical test target and the MTF of the XLV/scanner system was measured using x rays. From the measured MTF of the scanner, the theoretical MTF of the XLV/scanner system was established and compared with the experimental results. Good general agreement exists between experimental and theoretical results in the frequency range of interest for general radiography, although the theoretical curves slightly overstate the measured MTFs. The experimental MTF of the XLV was compared with the MTF of two clinical systems and was shown to have the capability to exceed the resolution of flat-panel detectors. From this, the authors can conclude that the XLV has an adequate resolution for general radiography. The XLV/scanner also has the potential to eliminate aliasing while maintaining a MTF that exceeds that of a flat-panel imager.
[DOI: 10.1118/1.2968093]

Key words: x-ray light valve, digital radiography, spatial resolution, modulation transfer function

I. INTRODUCTION

Digital radiography provides many advantages over traditional film-screen systems and a fully digital radiology department is desirable for all imaging tasks.[1] The current leading technology in digital x-ray systems in terms of image quality and dose to the patient is based on large area active matrix flat panel imagers (AMFPIs).[2] While AMFPIs provide excellent image quality and increased functionality over traditional film-screen systems, they are very expensive and are therefore used primarily for specialized procedures such as fluoroscopy,[3] cone-beam computed tomography (CT),[4] and digital tomosynthesis.[5] The most commercially successful digital radiographic x-ray systems are cassette-based computed radiography (CR) systems.[6] CR systems offer a more economical solution to digital radiography than flat-panels but at the cost of increased dose to the patient. The x-ray light valve (XLV) has been proposed[7,8] as a novel approach for a low-cost, high image quality digital radiographic imaging system. It is based on well-established and hence inexpensive technologies: Amorphous selenium (*a*-Se) as an x-ray to charge transducer and a liquid crystal (LC) cell as an analog image display.

The XLV consists of an *a*-Se layer and LC cell sandwiched between two bias electrodes (Fig. 1). Upon x-ray exposure, an optical image is created in the LC layer which can be digitized with an optical imager. Several variations on the design of the XLV system have been considered since its conception. Rieppo *et al.*[8] initially proposed a transmissive configuration in which the XLV can be considered to be a kind of x-ray image intensifier (XRII). It differed, however, from the electronic optical XRII, in that instead of generating and amplifying light created by x rays, the LC layer modulated the light from an external backlight, producing an amplification which depended on the exposure time of the readout light. In this arrangement, the optical image produced by the LC layer was coupled via a lens to a charge-coupled device (CCD) for readout. This arrangement required the readout light and CCD to be placed on opposite sides of the XLV and a large lens to focus the image, leading to a bulky device.[9] The use of an optical scanner and a reflective configuration has been proposed to reduce the size of the system and simplify readout.[10] By switching to a reflective LC cell, the light source and readout electronics can be confined to one side of the XLV. An optical scanner is used which mechanically scans a row of detector elements (dels), thus con-

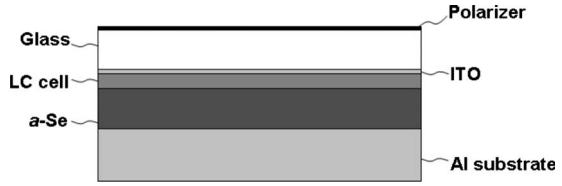

FIG. 1. Structure of an XLV: The XLV consists of an *a*-Se layer and LC cell in a sandwich structure. An Al and ITO glass substrate serve as the top and bottom electrodes to create the bias field across the entire structure. A polarizer is placed on top of the glass that modulates the intensity of readout light reflected onto detector elements in the scanner.

serving the pixel density of a static detector array, such as a CCD, while significantly reducing both the cost and bulk of the system. In this article, an XLV in combination with an optical scanner used in reflective mode for image readout is referred to as the XLV/scanner system.

The operation[10] of the XLV/scanner system to produce a digital radiograph involves three steps: Image formation, image digitization, and system reset. An overview of the operation of the XLV/scanner system is shown in Fig. 2. Each step is briefly described to provide a foundation for our discussion of spatial resolution. During x-ray exposure (step 1), a large bias potential is applied to the XLV which creates an electric field E across the entire structure. Incident x rays create electron-hole pairs in the photoconductive *a*-Se layer [Fig. 2(a)], then the electrons and holes move [Fig. 2(b)] to opposite surfaces of the photoconductor under the guidance of E, and electrons (or holes depending on field polarity) become trapped at the *a*-Se-LC interface, forming a latent charge image. After x-ray exposure, the bias potential is set to zero resulting in the bias field being removed. The charge image trapped at the *a*-Se-LC interface creates a spatially varying electric potential across the LC cell, resulting in a modulated LC latent image. In step 2 the LC latent image is made into a visible image by external illumination and polarizers. The analog image signal in the LC layer is pixelated by a detector array and digitized by an analog to digital converter using an optical scanner [Fig. 2(c)]. Finally in step 3, the XLV is reset by neutralizing the image charge to make the system ready for another exposure.

The spatial resolution of an imaging system is an important factor in determining image quality, and hence, the diagnostic accuracy for the radiologist. In direct-conversion AMFPIs, spatial resolution is based primarily on the pixel size of the detector since the inherent spatial resolution of the charge image is very high.[11] While smaller pixels allow for increased spatial resolution, a compromise is made in balancing the pixel size required for the diagnostic task with the cost of manufacturing the imaging system.[12] A ROC analysis conducted to determine the pixel size required to detect common abnormalities encountered in chest radiography[12] concluded that a pixel size of 200 μm is a satisfactory compromise. However, diagnostic accuracy of certain abnormalities was shown to increase with smaller pixel sizes down to 100 μm.[12] Flat-panel detectors in clinical systems for general radiography typically have pixel sizes in the range of 100–200 μm. Thus, in order for the XLV/scanner to be seen as a feasible system for general radiography, it should have an appreciable modulation transfer function (MTF) up to a spatial frequency of 5 cycles/mm corresponding to the Nyquist frequency of a 100 μm pixel.

In contrast to flat-panel detectors, the XLV is not an inherently pixelated device since the image formation and pixelation stages are separate processes. The spatial resolution of the XLV will be affected by the physical interactions in the photoconductive and LC layers. The x-ray interactions that result in the creation of charge in the photoconductive layer introduce a blur to the charge image formed at the *a*-Se-LC interface. An additional source of blur arises in the conversion of the charge image into an optical image in the LC layer. The spatial resolution of the XLV/scanner system will also be affected by the pixelation stage introduced by the scanner. We assume all of these stages to be independent in terms of their effects on spatial resolution of the system and are therefore analyzed separately in the following section.

A complete understanding of the factors affecting spatial resolution is required to assess the feasibility of the XLV for a digital radiography system as well as to optimize it for specific imaging tasks. The purpose of this article is to investigate the spatial resolution of the XLV by deriving a theoretical model which is validated by comparison with experimental results obtained with a prototype XLV.

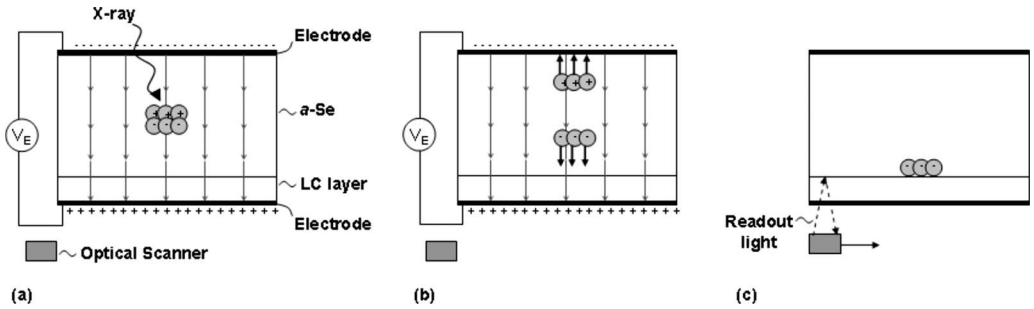

FIG. 2. Operation of the x-ray light valve. During x-ray exposure, a large bias potential (V_E) is applied. (a) X rays are absorbed in the *a*-Se layer generating a cloud of electron-hole pairs. (b) The large electric potential guides the electrons and holes to opposite surfaces of the photoconductor, ensuring minimal lateral spread of charge resulting in high spatial resolution. After the exposure is finished, the potential is removed and (c) the visible image induced in the LC cell by the electric field of the charges trapped at the *a*-Se surface is digitized by an optical scanner.

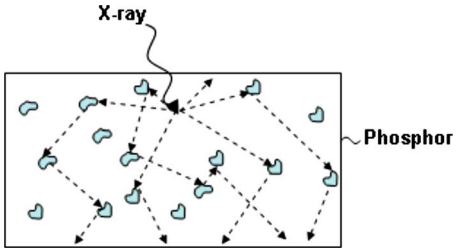

FIG. 3. Signal generation in a phosphor screen. The light emitted on x-ray absorption is scattered in the phosphor resulting in poor spatial resolution.

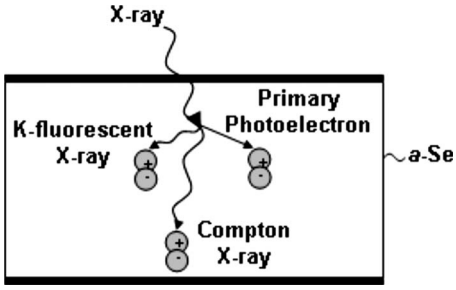

FIG. 4. Sources of blur in the photoconductor layer arising from x-ray interactions. X rays are either absorbed resulting in the ejection of a photoelectron and emission of a *K*-fluorescent x-ray in the case of a photoelectric interaction or become scattered in the case of a Compton interaction.

II. MODEL OF RESOLUTION FOR THE XLV

The spatial frequency dependent MTF is used to describe the spatial resolution characteristics of an x-ray imaging system. In order to perform MTF analysis, the system being studied must meet the requirements of linearity and shift invariance.[13]

The complete system MTF of an imaging system is the product of the MTF of each component in the imaging chain.[14] The component MTFs for the XLV/scanner system include the MTFs created by the physical interactions in the photoconductor (MTF_p) and LC cell (MTF_{LC}) as well as the optical scanner MTF (MTF_S). The MTF of the XLV (MTF_{XLV}) is thus the product of MTF_p and MTF_{LC},

$$MTF_{XLV}(v) = MTF_p(v) \cdot MTF_{LC}(v), \quad (1)$$

where v is spatial frequency. The total XLV/scanner system MTF ($MTF_{XLV/S}$) is the product of MTF_{XLV} and MTF_S,

$$MTF_{XLV/S}(v) = MTF_{XLV}(v) \cdot MTF_S(v). \quad (2)$$

Sources of blur in the photoconductor, LC, and optical scanner (readout) are described to provide a basis for the model used to calculate the theoretical MTF of the XLV.

II.A. Photoconductor MTF

Since the XLV is based on an electrostatic x-ray detector, it has the potential to create a high resolution latent charge image with layers thick enough to provide high quantum efficiency.[8] The presence of an electric field ensures there is very little resolution loss due to charge spread in the charge collection stage, making *a*-Se a higher resolution detector than phosphors, whose resolution limit (even in structured phosphors such as CsI) dominantly arises from optical spreading effects[6] as shown in Fig. 3. The process of charge image formation is described here and the sources of blur which affect MTF_p are introduced. MTF_p is defined as the MTF of the charge image stored on the surface of the *a*-Se layer.

In an electrostatic detector, a cloud of charge is created upon x-ray absorption, the average projected size of which we define as the intrinsic spatial resolution of the photoconductor layer. Charge which is created at some lateral (perpendicular to incident x rays) distance from the initial x-ray absorption site results in blurring of the charge image and a reduction in MTF_p. In *a*-Se, in the diagnostic energy range (10–100 keV), charge is created primarily upon photoelectric interactions. For example, the ratio between the photoelectric and Compton attenuation coefficients for x-ray energies of 40 and 80 keV are 57.7 and 7.4, respectively.

When an x-ray is absorbed by the photoelectric effect (Fig. 4), a photoelectron is ejected, typically from the *K* shell, with energy $E_0 - E_{BE}$ corresponding to the energy difference between the incident x-ray photon (E_0) and binding energy of the electron (E_{BE}). The vacancy created in the *K* shell is filled by outer-shell electrons resulting in the emission of a *K*-fluorescent x-ray with energy $E_K - E_L$ (if the vacancy is filled by an *L* shell electron) or the less probable ejection of an Auger electron with energy $E_K - 2E_L$. The low probability of ejection of an Auger electron combined with its low energy and hence short range make its effect negligible. However, *K*-fluorescent x-rays may travel some distance before being reabsorbed, creating charge away from the initial absorption site and significantly degrading the MTF. X rays which undergo Compton scattering may also create charge but this effect is not significant in *a*-Se due to the low probability of the Compton effect. Charge created in the bulk material, in this case *a*-Se, is guided by the electric field to form a charge image on the *a*-Se surface which reproduces the absorbed x ray intensity pattern.[10]

The intrinsic spatial resolution characteristics of *a*-Se have been investigated previously. Que *et al.*[11] used an analytic model to investigate seven different effects in *a*-Se. Of the seven effects considered, two were identified as being the most significant to the resolution of *a*-Se over a large frequency span (up to 100 cycles/mm): The range of primary photoelectrons and the geometric effect. The range of photoelectrons has been described and is a result of photoelectric interaction. The geometric effect arises from the non-normal incidence of x rays which are absorbed at some lateral distance from the point at which they entered the *a*-Se layer. Both these effects have an energy dependence that is reflected in a degradation of the MTF at higher incident x-ray energies. However, in practical measurements of the MTF, the geometric effect can be avoided by measuring the MTF of the detector at the central axis of the x-ray beam. Therefore, for validation of the theoretical model with experimental results and for comparison of the MTF of the XLV with existing systems, the geometric effect is excluded. However, this effect does become significant at the edges of a practical

detector when the angle of the incident x-ray beam becomes significant (>10°) and the effect will be the same in both the XLV and AMFPIs. However, we may conclude that for normal incidence, the range of photoelectrons is the dominant effect on MTF.

Hadjok *et al.*[15] presented a cascaded model of the photoelectric effect to describe signal transfer in terms of the MTF. The authors compared results from a theoretical model with Monte Carlo calculations for an *a*-Se based x-ray converter. The results from the Monte Carlo calculations were taken to be the true photoelectric MTF since the authors considered that the cascaded model overstated the MTF at high energies (80 keV) when electron range becomes significant. The most significant effect for spatial frequencies <10 cycles/mm was found to be the reabsorption of *K*-fluorescent x-rays. Below the *K* edge of Se (12.66 keV), *K* fluorescence is absent and the reabsorption of *L*-fluorescent x-rays creates a negligible effect on the MTF. Just above the *K* edge, reabsorption results in a drop in MTF at low spatial frequencies (by 25% at 10 cycles/mm). The effect decreases with increasing energy and the MTF at high energies (80 keV) approaches the MTF at energies below the *K* edge at low spatial frequencies. At high spatial frequencies (>10 cycles/mm) and high photon energies (80 keV), the range of primary photoelectrons degrades the MTF, in agreement with the results presented by Que *et al.*[11]

From this review, we see that the inherent spatial resolution of *a*-Se is controlled by x-ray interactions, namely reabsorption of *K* fluorescence for low spatial frequencies (<10 cycles/mm) at energies near the *K* edge and the range of primary photoelectrons for high spatial frequencies (>10 cycles/mm) and high photon energies.

II.B. Liquid-crystal cell MTF

LC displays are known to achieve high resolution in large area devices for a wide range of applications.[16] Here, we consider the resolution limits of a LC cell in creating an x-ray image in an XLV. The LC cell that has been proposed[17] for use in the XLV is based on electrically controlled birefringence (ECB) and is know as a reflective-ECB (*r*-ECB) cell, similar to those used in reflective liquid-crystal displays.[18] Fundamental to image formation are the optical and dielectric anisotropies of individual LC molecules.[10] The dielectric anisotropy ($\Delta\varepsilon$) defined as the difference in dielectric constants between the parallel direction, $\varepsilon\|$, and direction perpendicular to the long axis of the LC molecule, $\varepsilon\perp$, causes the molecules to rotate and align their long axis with an applied electric field. The optical anisotropy, which depends on the orientation of the LC molecules, affects the propagation of light through the cell. Thus, spatial variations in the charge image cause spatial variations in the intensity of the readout light so that the optical image created in the LC cell reproduces the absorbed x-ray energy pattern.[10]

The main sources of blur in the LC layer are considered here to determine MTF_{LC}. These are the MTFs created by: (i) The finite size of individual LC molecules (MTF_{MOL}); (ii) the effect of electric field spreading across the LC layer (MTF_{FS}); and (iii) the angle of incidence of the readout light (MTF_{θ}). These effects are illustrated in Fig. 5. The LC cell MTF may then be expressed as

$$MTF_{LC}(v) = MTF_{MOL}(v) \cdot MTF_{FS}(v) \cdot MTF_{\theta}(v). \quad (3)$$

Each effect is considered separately to identify the magnitude of each and to calculate MTF_{LC}.

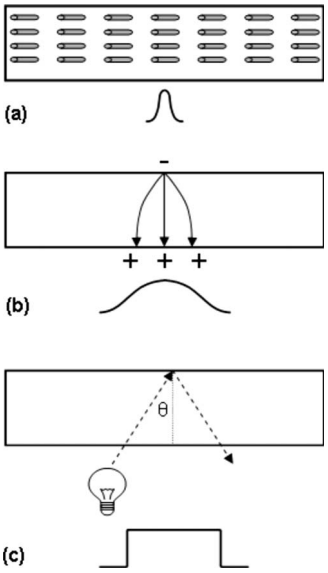

FIG. 5. Sources of blur in the LC layer and qualitative line spread functions resulting from: (a) The finite size of individual LC molecules (MTF_{MOL}), (b) the effect of field spreading (MTF_{FS}) across the LC layer, and (c) the incident angle of readout light (MTF_{θ}). The only significant effect is that of field spreading in the LC layer.

II.B.1. Size of LC molecules

The LC cell is composed of many LC molecules [Fig. 5(a)]. The size of individual LCs is typically very small (10–100 nm) since they possess a simple molecular structure consisting of only several organic chains.[19] As a rough estimate, MTF_{MOL} is expected to have an appreciable value over the frequency span of $\sim 1/(1\times10^{-4}\ \text{mm}) = 10\,000$ cycles/mm. Therefore, the effect of MTF_{MOL} on MTF_{LC} is expected to be quite small.

II.B.2. Field spreading

Field spreading in the LC layer [Fig. 5(b)] has the potential to be a significant source of blur in the XLV. In a LC cell, individual LC molecules possess an electrical polarizability which allows them to align with an applied *E*, resulting from either a bias potential, as in displays, or from a charge distribution as in the case of the XLV. The transmission of the LC cell is affected by the orientation of all the LC molecules throughout the layer. However, the transmission of an LC cell can be determined[19] from the voltage across the layer arising from *E*. Therefore, for an LC cell free of impurities, we do not need to be concerned with the orientation of *E* across the LC cell, only the effective voltage created by this field. For the geometry consisting of a photoconductor and

dielectric layer (LC cell) sandwiched between two bias electrodes, the solution for the potential across the LC layer arising from a sinusoidal charge distribution with surface charge density

$$\sigma = \frac{\sigma_0}{2}\left(1 + \cos\frac{2\pi}{\lambda}y\right) \tag{4}$$

at the photoconductor surface, where λ is the wavelength of the charge distribution, is given by Schaffert[20]

$$V_{LC}(v) = B + B_0 z + [B_1(v)e^{p(v)z} + B_2(v)e^{-p(v)z}]\cos[p(v)y], \tag{5}$$

where the coefficients are

$$B = \left(\frac{\varepsilon_b}{\varepsilon_a} - 1\right)B_0 d_p + \frac{\sigma_0 d_p}{2\varepsilon_a},$$

$$B_0 = \frac{\varepsilon_a V_0 - \sigma_0 d_p/2}{\varepsilon_b d_p + \varepsilon_a(d_{LC})},$$

$$B_1(v) = \frac{-\sigma_0 e^{-p(v)(d_p+d_{LC})}\sinh[p(v)d_p]}{4p(v)\{\varepsilon_{LC}\sinh[p(v)d_p]\cosh[p(v)d_{LC}] + \varepsilon_p\cosh[p(v)d_p]\sinh[p(v)d_{LC}]\}},$$

$$B_2(v) = -B_1(v)e^{2p(v)(d_p+d_{LC})},$$

where z is the distance into the LC layer from the a-Se-LC interface, y is the distance along the interface, $p(v)=2\pi v$, where v is the spatial frequency of the sinusoidal charge distribution, and ε_{LC}, ε_{Se}, d_{LC}, and d_{Se} are the dielectric constants and thicknesses of the LC and a-Se layers, respectively. The coefficients B and B_0 represent the mean voltage and can therefore be eliminated to give the spatial frequency dependent voltage modulation at the a-Se-LC interface ($z=0$),

$$V_{LC}(v) = B_1(v) + B_2(v). \tag{6}$$

Normalizing Eq. (5) to the voltage modulation at low spatial frequency (0.1 cycles/mm) gives the MTF due to field spreading in the LC cell

$$\mathrm{MTF}_{FS} = \frac{V_{LC}(v)}{V_{LC}(0.1)}. \tag{7}$$

This normalization factor $V_{LC}(0.1)$ is a valid zero-frequency approximation since MTF_{FS} has an essentially flat response below 1 cycles/mm. Using Eqs. (6) and (7) we have calculated the MTF due to field spreading for various values of d_{LC} and it is shown that the effect of field spreading is more significant for a thicker LC layer (Fig. 6).

II.B.3. Incidence angle of readout light

The incident angle of the readout light [Fig. 5(c)] used to pixelate the optical image in the LC cell introduces an additional blur to MTF_{LC}. The distance between the entrance and exit points of the readout light creates a blur in the optical image created in the LC cell. MTF_{θ} is shown for three angles in Fig. 7, where we assume the MTF_{θ} to arise from a rectangular pixel aperture function determined by the distance between the entrance and exit point of readout light. We have assumed a refractive index of 1.4794 for the LC cell which represents the minimum value for the LC mixture[18] used, and hence, the worst case scenario for blurring. For the incident angle used in the optical scanner (22.5°),[17] this effect is very small.

II.B.4. Total MTF of the LC cell

Three effects were considered which may contribute to a loss in MTF of the LC cell: The size of LC molecules

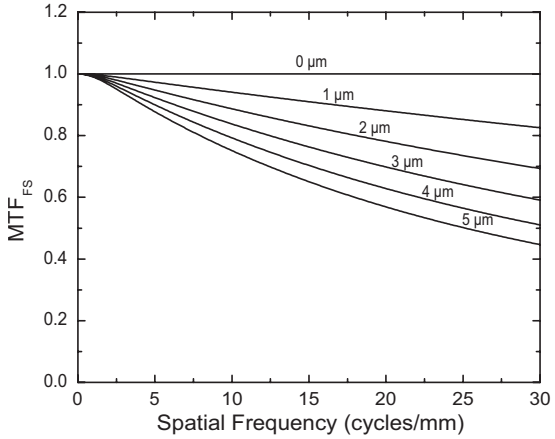

FIG. 6. LC cell MTF due to field spreading [Eq. (7)] calculated as a function of LC thickness (0–5 μm). MTF_{FS} degrades as the LC cell thickness is increased.

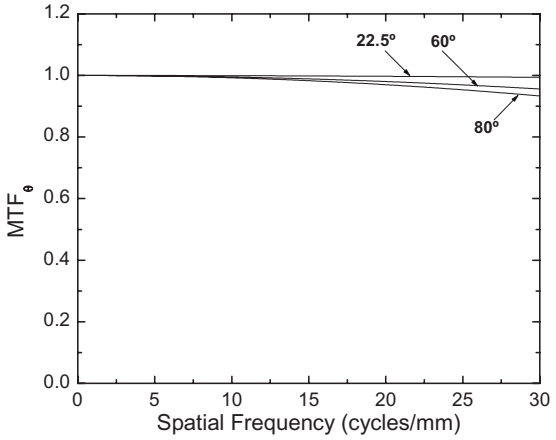

FIG. 7. The effect of MTF_θ on MTF_{LC} for three angles of incidence of the readout light. This effect is negligible for the angle of incidence used in the prototype XLV (22.5°).

(MTF_{MOL}), field spreading across the LC cell (MTF_{FS}) and the effect of the incident angle of readout light (MTF_θ). The size of the LC molecules are very small (10–100 nm) corresponding to a large frequency range (10 000 cycles/mm) for MTF_{MOL}. MTF_{FS} has been shown to cause a decrease in MTF_{LC} and the magnitude of this effect depends on the thickness of the LC cell. From Fig. 7, MTF_θ is almost ideal for all practical angles of readout light (<45°) and so is not expected to degrade MTF_{LC}. From this analysis, of the three components contributing to resolution loss, we have shown the effect of field spreading to be the only important factor affecting the resolution of the LC cell up to a spatial frequency of 30 cycles/mm, the highest frequency considered.

II.C. Optical scanner MTF

The optical image created in the XLV is digitized with an optical scanner which reads out a row of the image with a light source, optical readout lenses, and a row array of dels in the fast-scan direction. An image of the XLV is obtained by scanning this optical assembly (scanhead) across the face of the XLV in the slow-scan direction. There are three factors affecting the spatial resolution of the optical scanner: The pixel aperture function introduced by the dels, the readout optics and, in the slow-scan direction, motion blur. The pixel aperture function in the fast-scan-direction (i.e., along the linear array of dels) corresponds to the size of the dels in the scanhead. In the slow-scan-direction, the aperture function is defined by the step distance of the scanhead convolved with the del aperture. The readout optics in the optical scanner introduce blur due to imperfect focusing, arising from diffraction and lens aberrations, of the readout light onto the dels. The light source emits light from a light emitting diode (LED) light pipe onto the region of the XLV surrounding the scan line. The specularly reflected light at the *a*-Se-LC interface and reaching the input of the gradient index (GRIN) lenses is focused onto a del by the GRIN lens array onto the scanhead. These lenses have a depth of field of ~1.5 mm. A detailed analysis[9] of an off-the-shelf optical scanner showed the GRIN optics to be the dominant factor limiting the spatial resolution of the scanner. In the XLV/scanner prototype, a modified scanner was used but we expect the effect of blurring caused by the GRIN lenses to be similar. In contrast to *a*-Se and LC where the resolution is limited by fundamental physics, the optical scanner is limited by certain subcomponents (e.g., GRIN lenses) which can be replaced.

III. METHODS AND MATERIALS

An XLV prototype was constructed[10] for the purpose of measuring the experimental $MTF_{XLV/S}$. The structure of the prototype XLV is shown in Fig. 1. The active region of the XLV consisted of a 3.8 μm-thick *r*-ECB cell (LC mixture ZLI-4792) and a 150 μm-thick *a*-Se layer, both sandwiched between two conducting bias electrodes. The LC bias electrode consisted of a transparent indium tin oxide layer coated onto a 0.5 mm-thick glass substrate which was biased positively. The *a*-Se was evaporated onto a 2.1 mm-thick aluminum substrate which also provided the negative bias electrode.

A previous analysis[17] of the ECB cell used in the prototype XLV has shown that the LC cell exhibits a multivalued optical response and thus a nonmonotonic characteristic curve. At the bottom of the characteristic curve, the LC cell appears black and the XLV is in a black state. A bias potential applied to the LC cell has been shown to shift the characteristic curve to this black region, resulting in a monotonically increasing characteristic curve. This bias potential can be achieved either with an applied voltage or an appropriate x-ray exposure. In this article, a flood x-ray exposure was used to shift the characteristic curve to a monotonic region and to bring the XLV to a black state prior to the image exposure. By using a thinner LC cell, the characteristic curve could be optimized so as to be monotonically increasing without a prior bias potential and thus this issue is not seen as a limitation to the operation of the XLV system as a clinical device.

For digitization of the XLV optical image, a commercial document scanner (CanoScan LiDE30, Canon, Inc.) was used. The moving scanhead was modified to accept specularly reflected light from the smooth *a*-Se surface as the light passes from a low refractive index material (LC) to a high refractive index material (*a*-Se) at the *a*-Se-LC interface. This is different from off-the-shelf scanners which use diffusely scattered light for paper scanning. The scanner was operated in its full native resolution of 1200 dpi (21.17 μm pixel pitch), controlled by in-house software and readout in 8-bit mode. The illumination of the scanner was modified and consisted of three red LEDs, having a peak emittance at 655 nm.

To measure the characteristic curve of the XLV prototype, the XLV was placed 1.65 m from the tungsten target x-ray source, which was operated at 60 kVp with 2 mm added Al filtration. Before reaching the *a*-Se layer, the radiation passed through a further 2.1 mm of Al substrate of the *a*-Se. The potential applied to the XLV during x-ray exposure was 1500 V, corresponding to a calculated electric field of

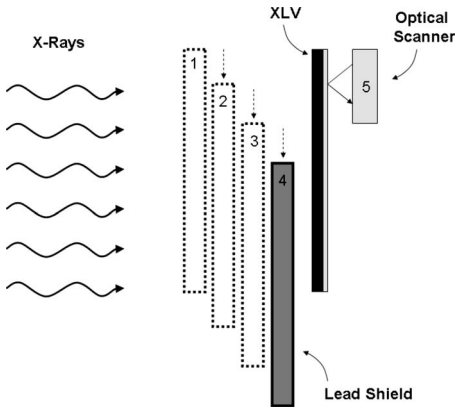

FIG. 8. A schematic of the experimental setup used to obtain the characteristic curve of the XLV. A lead (Pb) shield was placed between the x-ray beam and the XLV. The shield was moved at discrete intervals using a stepper motor (1–4) and the XLV was exposed at each step to form a simulated step wedge. The XLV was then read out as a single image and the characteristic curve was obtained by averaging the pixel values in each step.

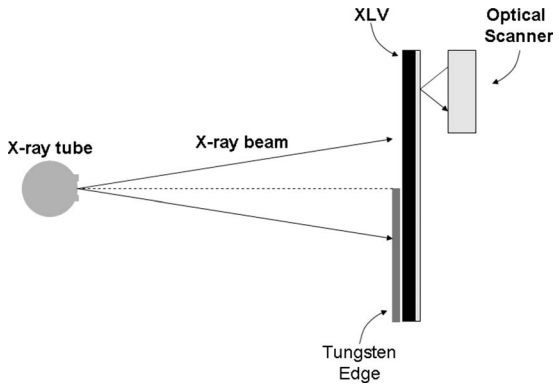

FIG. 9. A schematic of the experimental setup used to measure the MTF of the XLV/scanner system. A tungsten edge was placed in close proximity (~1 cm) to the XLV along the central axis of the x-ray beam. The edge was placed at 1.5° relative to the scanner dels to obtain an oversampled edge image. The image was readout with an optical scanner and the MTF was obtained from the oversampled edge image using standard techniques (Ref. 21).

10 V/μm in the *a*-Se layer. Prior to the image exposure, the biased XLV was exposed to a flood x-ray exposure in order to bring the LC cell to a black state. In order to measure the characteristic curve, the XLV was exposed with a simulated lead step wedge to form 11 steps including a region of no added exposure (Fig. 8). The time for one exposure step was ~10 s corresponding to ~100 s for all ten exposures. Image decay was assumed to be minimal in this time frame. The step wedge image was then readout as a complete image. The data points for the different x-ray exposure steps were obtained by averaging pixels within each step. The incident exposure at the XLV plane was established using an ionization chamber (Inovision, model 35040) averaged over several measurements to obtain accurate absolute exposure values. For this measurement, an additional 2.1 mm-thick Al plate was placed in front of the chamber to account for attenuation and scattering of the Al *a*-Se substrate and the XLV was removed to prevent backscatter from the *a*-Se and Al substrate. The exposure at each step was calculated from the exposure reading for a given mAs tube setting.

The experimental MTF of the XLV/scanner system and optical scanner alone were measured in both the fast-scan and slow-scan directions using the oversampled edge technique.[21] An image of a tungsten edge, placed at an angle of 1.5° relative to the scanner array in both directions, was obtained with a 60 kVp (4.1 mm Al filtration) and 120 kVp (0.5 mm Cu+4.1 Al filtration) spectrum (Fig. 9). From this point forward, the spectra will simply be referred to in terms of beam energies, but include the filtration mentioned above. The center of the edge was located on the central axis of the x-ray tube and at a distance of 1.65 m from the focal spot. In order to minimize focal spot blurring, the XLV to edge distance was kept very small (~1 cm) in comparison to the source-to-image distance.

The MTF of the optical scanner was measured in both the fast-scan and slow-scan directions by replacing the XLV with a very high spatial resolution reflective target (Newport Corporation, NRC) which consisted of a reflective chromium bar pattern on a clear background. The edge of one bar was used and was assumed to be perfect since the target contained microscopically resolvable bar patterns with pitches up to 200 lp/mm. The edge was placed at ~1.5° to the scanner dels in both directions and the target was scanned. The resulting images were cropped to obtain edge images. The corresponding oversampled edge spread function (ESF) and MTF were obtained using standard methods.[21]

IV. RESULTS

Theoretical calculations were performed for x-ray energies of 40 and 80 keV to represent the two ends of the diagnostic radiography energy range. To verify the model, the experimental MTF was measured for two x-ray spectra, 60 and 120 kVp, chosen so that the mean energies corresponded to the energies used to obtain the theoretical results. The mean energies were calculated by obtaining the x-ray spectra by the method outlined by Tucker[22] and were found to be 39.4 and 70 keV. For clarity, theoretical MTFs will be denoted as MTF and experimental MTFs will be denoted with a prime (i.e., MTF′).

MTF_{XLV} was obtained from MTF_{LC}, derived from Eqs. (6) and (7), and MTF_p as calculated by Hadjok *et al.*[15] for x-ray energies of 40 and 80 keV, using Eq. (1). MTF_{LC} is calculated using the same parameters obtained from our experimental prototype, namely $d_{LC}=3.8$ μm, $d_p=150$ μm, $\varepsilon_{LC}=6.7$, and $\varepsilon_p=6.3$. Figure 10 shows the contributions of each component, which are comparable although MTF_p exceeds MTF_{LC} at all spatial frequencies.

Figure 11 compares MTF_{XLV} for the two incident photon energies. There is no difference between the 40 and 80 keV results up to a spatial frequency of ~10 cycles/mm where the two curves begin to diverge. This is because the effect of electron transport becomes significant at higher photon energies.[15]

Before measuring $MTF'_{XLV/S}$, we have to ensure that the conditions for linear systems analysis are met. Since the LC

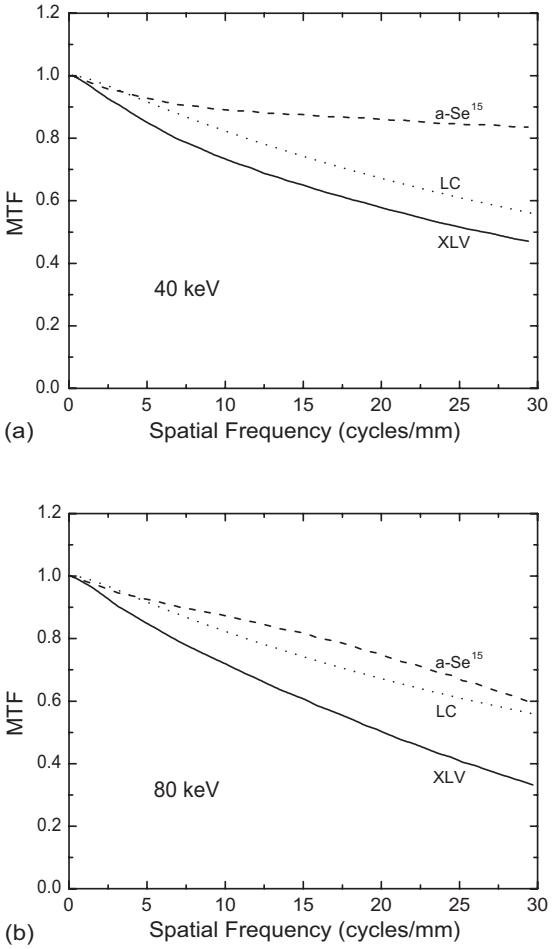

FIG. 10. Theoretical calculations for MTF_p, MTF_{LC}, and $MTF_p \times MTF_{LC}$ (i.e., MTF_{XLV}) for x-ray energies of (a) 40 and (b) 80 keV.

cell has an almost uniform thickness and corrections are made to account for nonuniformities, we can assume an isotropic response and, therefore, the system to be shift invariant. However, it is necessary to establish the linearity of the XLV/scanner system. To verify this, the characteristic curve

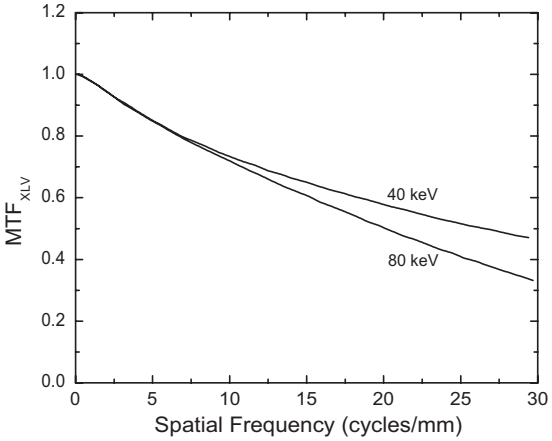

FIG. 11. Theoretical MTF_{XLV} for incident x-ray energies of 40 and 80 keV. MTF_{XLV} decreases more rapidly for the 80 keV case than 40 keV due to the large range of electrons in the former case.

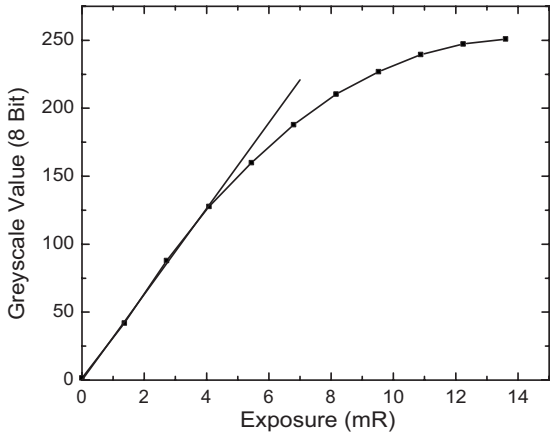

FIG. 12. Characteristic curve of the XLV. The XLV has a linear response over the range of 0–6 mR.

of the XLV was measured (Fig. 12). From the figure, it is evident that the XLV responds linearly over the exposure range of 0–6 mR, yielding $R^2 > 0.99$ from linear regression analysis. Therefore, by keeping the exposures <6 mR, the condition of linearity of the system is satisfied.

MTF'_S is shown in Fig. 13. As expected from previous analysis,[9] the optical scanner adds an additional blur to the XLV/scanner system. MTF'_S is higher in the fast-scan direction most likely due to motion blur in the slow-scan direction.

$MTF'_{XLV/S}$ was measured for 60 and 120 kVp spectra in both scan directions (Fig. 14). Due to the high resolution of the XLV, we notice an energy dependence on $MTF'_{XLV/S}$, which is slightly higher for the 60 kVp beam energy. The ESF and LSF corresponding to $MTF'_{XLV/S}$ measured at 60 kVp in the fast-scan direction are shown in Fig. 15. An x-ray image of a lead star phantom acquired with the XLV/scanner at 60 kVp is shown in Fig. 16. In the fast (horizon-

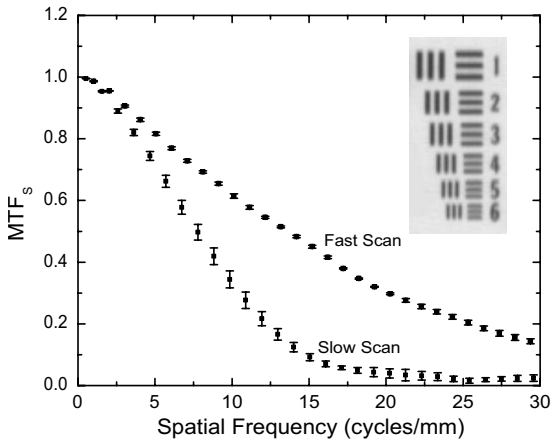

FIG. 13. Plot of MTF'_S measured with an optical edge method. The error bars represent the standard error of the mean obtained from five independent measurements. Inset: View of optical resolution target (Newport Corporation, NRC) read-out with the optical scanner demonstrating blur. The numbered bar patterns correspond to spatial frequencies of: (1) 8, (2) 8.98, (3) 10.08, (4) 11.31, (5) 12.70, and (6) 14.25 lp/mm in both the fast- (horizontal) and slow- (vertical) scan directions.

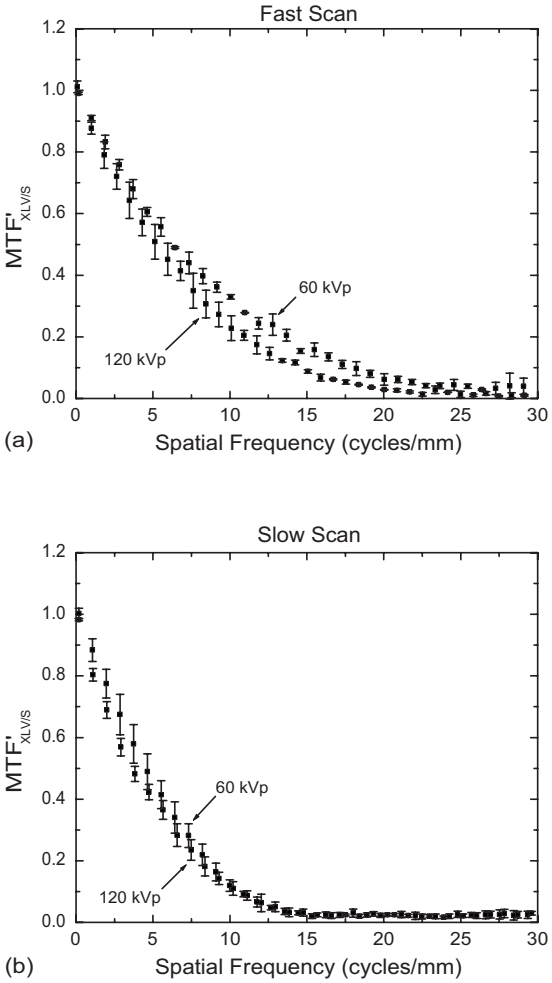

FIG. 14. $MTF'_{XLV/S}$ measured for 60 and 120 kVp x-ray spectra. There is a slight energy dependence resulting in a lower $MTF'_{XLV/S}$ at 120 kVp. The error bars represent the standard error of the mean obtained from five independent measurements.

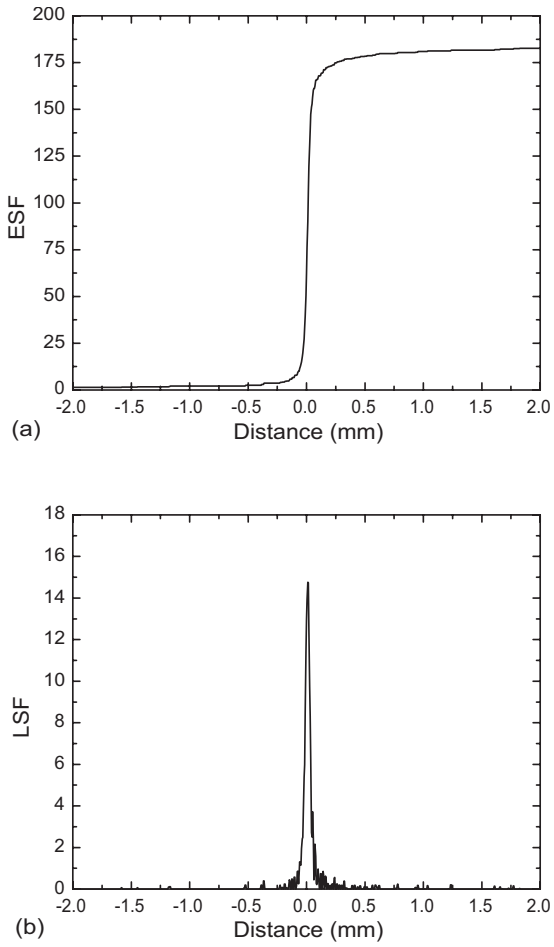

FIG. 15. ESF and LSF corresponding to $MTF'_{XLV/S}$ measured at 60 kVp in the fast scan direction.

tal) scan direction, the bars at the center of the star pattern corresponding to a spatial frequency of 11.4 cycles/mm, are easily distinguished. It is more difficult to distinguish individual bars in the slow (vertical) scan direction at the center of the pattern, in agreement with the results presented in Fig. 14.

V. DISCUSSION

Theoretical calculations were performed in order to establish MTF_{XLV} from MTF_p and MTF_{LC}. For MTF_p, monoenergetic x rays were used to approximate the x-ray spectrum. The theoretical results for a monoenergetic beam would have a tendency to overstate the actual MTF for a spectrum. This is because below the mean energy, *K* fluorescence is weighted more heavily, thus causing a low frequency drop and above the mean energy, electron range becomes larger, causing a greater drop at high frequencies. At 10 cycles/mm, the error introduced from this approximation is mainly due to the contribution of *K* fluorescence from lower energy photons in the spectrum. A maximum error of ~10% in MTF was estimated by comparing the MTFs for 13 and 40 keV obtained by Hajdok *et al.*[15] at 10 cycles/mm. This represents the maximum error since the photoelectric MTF peaks (for energies above the *K* edge) at roughly 40 keV and is lowest just above the *K* edge at 13 keV. The biggest difference oc-

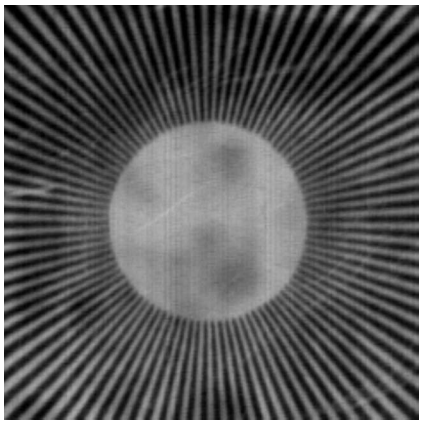

FIG. 16. Image of a lead star phantom obtained with the XLV/scanner system at 60 kVp. The light regions correspond to areas of lead. At the center of the pattern, the spatial frequency is 11.4 cycles/mm. This is easily resolved in the fast scan (horizontal) direction, but is more difficult to see in the slow scan (vertical direction).

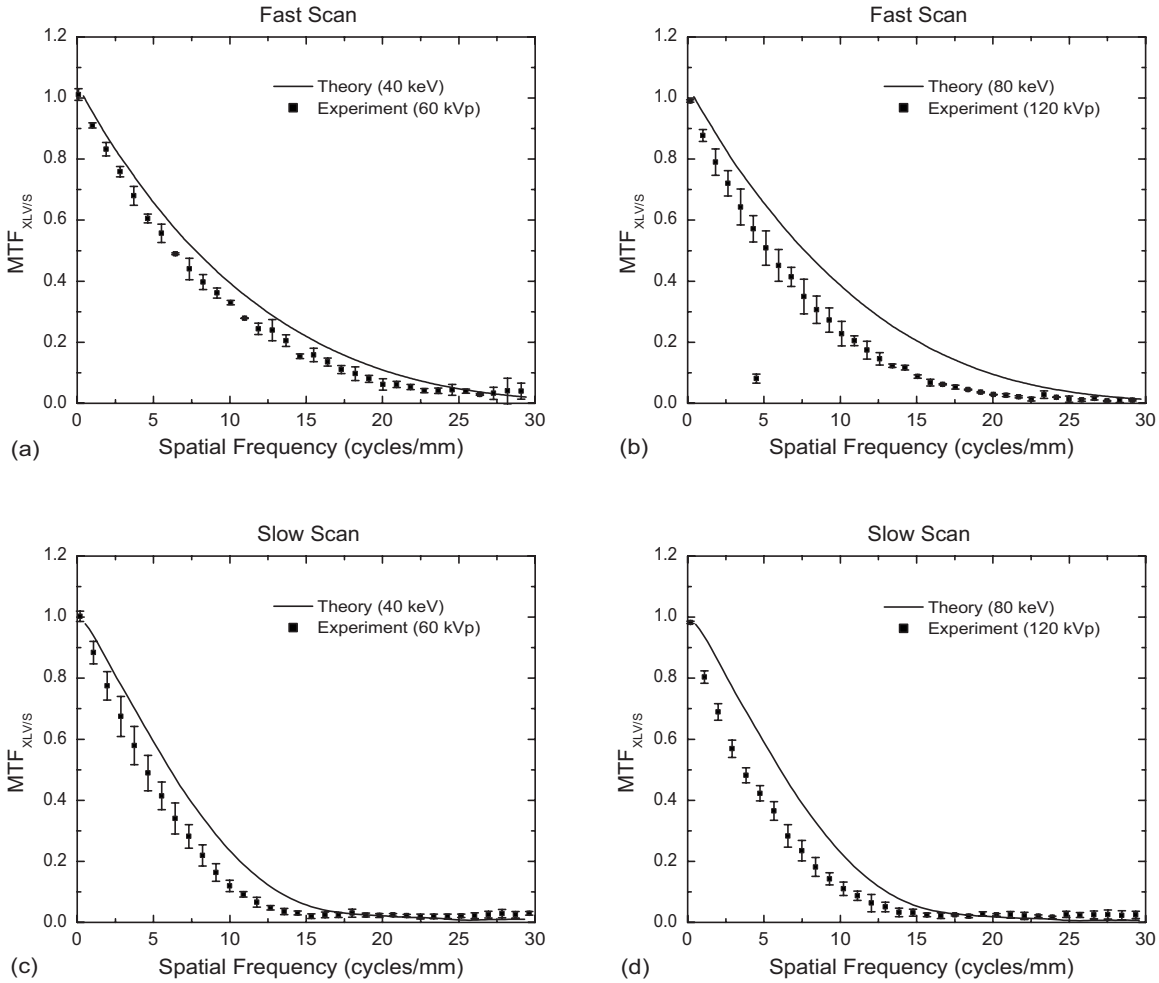

FIG. 17. Comparison between $MTF_{XLV/S}$ and $MTF'_{XLV/S}$ for [(a), (c)] 60 and [(b), (d)] 120 kVp in the fast- [(a), (b)] and slow [(c), (d)] scan directions. The error bars represent the standard error of the mean obtained from five independent measurements.

curs at ~10 cycles/mm. At higher energies, electron transport begins to degrade the MTF and begins to approach the MTF for 13 keV.

For the 60 kVp beam, there is virtually no x-ray fluence for energies in the 13 keV range due to the filtration of the beam prior to reaching the *a*-Se layer (4.1 mm Al total). Even at energies of 20 keV, the fluence is ~3% of that for 40 keV photons. These fluence values were calculated by obtaining the x-ray spectra from the method outlined by Tucker.[22] For the 120 kVp beam, the error resulting from the mean energy approximation is even less significant. Therefore, the errors involved are negligible and the mean energy approximation is valid.

MTF_p was taken as the photoelectric MTF in the *a*-Se layer, and so did not include the effects of Compton scattering or blur in the charge collection stage. Blur in the charge collection stage has been shown to be negligible for the bias field used on the prototype (10 V/μm).[11] The effect of Compton scattering is negligible in the *a*-Se layer but could have an effect in the Al substrate in direct contact with the *a*-Se layer. We can obtain an estimate of the MTF of the Al layer and the effect of Compton scattering by estimating the fraction of incident x rays scattered by the Compton effect. The Compton mass attenuation coefficients for Al at 40 and 80 keV are 0.149 and 0.144 cm^2/g, respectively, corresponding to approximately 8% of incident photons interacting through the Compton effect in the 2 mm-thick Al layer. If we assume half of these to be forward scattered and interacting in the *a*-Se layer, this corresponds to a 4% drop in MTF, since the Compton MTF drops quickly to approximately 0.2 at 5 cycles/mm and 0.1 at 10 cycles/mm.[11]

For the theoretical calculation of MTF_{XLV}, MTF_{LC} was shown to be the most significant factor limiting MTF_{XLV} at high spatial frequencies (>10 cycles/mm) in the 40 keV case [Fig. 10(a)]. This is at first sight somewhat surprising, given the relatively small thickness (3.8 μm) of the LC layer. However, field spreading even across this distance is considerable. At 80 keV [Fig. 10(b)], MTF_p is lower than at 40 keV and drops close to the value of MTF_{LC} over all spatial frequencies which results in a lower MTF_{XLV}.

MTF'_S and $MTF'_{XLV/S}$ were obtained several times which resulted in a range of MTF curves. The standard error of the mean obtained from 5 curves was used to obtain the error bars at each spatial frequency for both MTF'_S (Fig. 13) and $MTF'_{XLV/S}$ (Fig. 14).

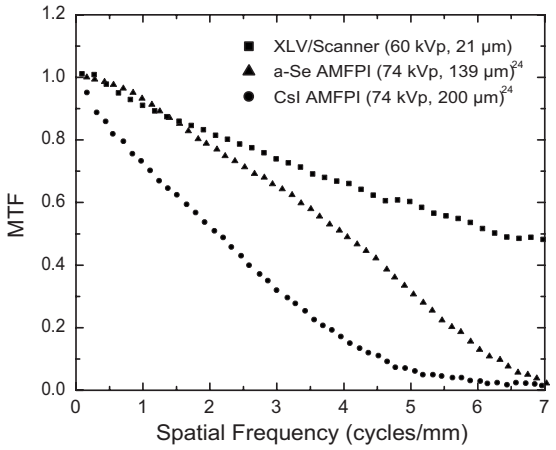

FIG. 18. Comparison between the presampled MTFs of a direct (*a*-Se, 139 μm pixel pitch) and indirect conversion (CsI, 200 μm pixel pitch) flat-panel detector and the XLV (21 μm pixel pitch). The MTF of the XLV exceeds that of flat-panel imagers and its resolution is adequate for general radiography.

The theoretical MTF of the XLV/Scanner system ($MTF_{XLV/S}$) was obtained by multiplying MTF_{XLV} (Fig. 10) with MTF'_S in both directions. $MTF_{XLV/S}$ is compared with $MTF'_{XLV/S}$ for the two beam energies and scan directions in Fig. 17. $MTF'_{XLV/S}$ measured at 60 kVp is in good general agreement with the theoretical curve in both scan directions. If we consider 5 cycles/mm to be the highest spatial frequency of interest for general radiography, the difference between the theoretical and experimental results at this frequency are ~5% and ~13% for the fast- and slow-scan directions respectively. However, for the higher energy, $MTF'_{XLV/S}$ (120 kVp) is lower than the theoretical prediction in both scan directions. At 5 cycles/mm, the experimental results are within ~13% and ~17% of the theoretical values for the fast- and slow-scan directions, respectively. Thus, the energy dependence seen in the experimental results cannot be fully explained by x-ray interactions in the *a*-Se layer, namely electron transport. Other possible reasons for this discrepancy between experimental and theoretical values include Compton scattering in the Al substrate of the XLV, charge trapping in the *a*-Se layer,[23] and backscatter from the glass in the optical scanner. Compton scattering has been discussed and shown to cause a decrease in MTF, albeit independent of x-ray energy. Although this is a source of blur for the prototype used in this article, this would not be the case in a real system since the *a*-Se layer could be evaporated onto another material such as glass. Charge trapping, or incomplete charge collection, is known to decrease the sensitivity of a direct-conversion detector and is referred to as ghosting. However, charge trapping has also been shown to cause a decrease in MTF for a negatively biased detector,[23] such as the XLV. Due to the relatively small thickness of the *a*-Se layer (150 μm), this effect is expected to be quite small in our prototype. Another possible explanation is x-ray backscatter from the glass in the optical scanner, which is in direct contact with the XLV. This effect is energy dependent, leading to a decrease in MTF at higher energies, which we see in our experimental results.

The presampled MTFs of the XLV/scanner in the fast-scan direction, a direct conversion AMFPI and indirect conversion AMFPI[24] are compared in Fig. 18 to assess the feasibility of the XLV/scanner as a detector for general radiography. The $MTF'_{XLV/S}$ exceeds that of the direct conversion *a*-Se based detector and indirect conversion CsI-based detector measured for approximately equivalent x-ray spectra. Therefore, we can conclude that the XLV has adequate resolution for general radiography.

The XLV/scanner system has the unique capability to sample the charge image created in the photoconductor at much higher spatial frequencies than a flat-panel detector. Unlike a direct-conversion AMFPI system, the MTF of XLV/scanner system is not limited by a large pixel size (i.e., 139 μm), thus providing an opportunity to reduce aliasing in the digital radiograph. The pixel size in the optical scanner is 21 μm. In the case of an *a*-Se-based flat-panel detector, this pixel size would still be large enough to introduce aliasing due to the high intrinsic resolution of selenium.[11] However, in the XLV/scanner, a built-in presampling filter exists since the LC cell and readout optics in the scanner act to blur the sharp charge image present on the *a*-Se surface, thereby eliminating aliasing artifacts in the digital radiograph. This can be seen in Fig. 14 where $MTF'_{XLV/S}$ is essentially zero beyond the Nyquist frequency (23.8 cycles/mm for a 21 μm pixel).

VI. CONCLUSIONS

The spatial resolution of an XLV was investigated with a theoretical model which was compared with experimental measurements of MTF. The theoretical model tends to overstate the system MTF, particularly at higher energies. For the results obtained at 60 kVp, good general agreement exists between the theoretical and experimental values over the spatial frequency range of interest for general radiography. At 120 kVp, the discrepancy between the theoretical and experimental results is more pronounced. Possible reasons for this discrepancy include Compton scatter in the Al substrate as well as x-ray backscatter from the glass in the optical scanner. Based on a comparison with commercial flat-panel detectors, the resolution of the XLV/scanner system was shown to be adequate for general radiography. We have also shown the XLV/scanner system to have the potential to significantly reduce aliasing present in flat-panel detectors while exceeding the MTF of such systems.

ACKNOWLEDGMENT

This work was supported by the National Institute of Health Grant no. 5-R01-EB-002-352-02, "Low cost digital x-ray detectors using liquid crystals."

[a]Electronic mail: john.rowlands@sunnybrook.ca

[1]J. A. Rowlands and J. Yorkston, "Flat panel detectors for digital radiography" in *Handbook of Medical Imaging, Vol. 1. Physics and Psychophysics*, edited by J. Beutel, H. L. Kundel, and R. L. Van Metter (SPIE,

Bellingham, WA, 2000), pp. 223–328.
[2]M. J. Yaffe and J. A. Rowlands, "X-ray detectors for digital radiography," Phys. Med. Biol. **42**, 1–39 (1997).
[3]D. C. Hunt, O. Tousignant, and J. A. Rowlands, "Evaluation of the imaging properties of an amorphous selenium-based flat panel detector for digital fluoroscopy," Med. Phys. **31**, 1166–1175 (2004).
[4]D. A. Jaffray and J. H. Siewerdsen, "Cone-beam computed tomography with a flat-panel imager: Initial performance characterization," Med. Phys. **27**, 1311–1323 (2000).
[5]J. G. Mainprize, A. K. Bloomquist, M. P. Kempston, and M. J. Yaffe, "Resolution at oblique incidence angles of a flat panel imager for breast tomosynthesis," Med. Phys. **33**, 3159–3164 (2006).
[6]J. A. Rowlands, "The physics of computed radiography," Phys. Med. Biol. **47**, R123–R166 (2002).
[7]I. Koprinarov, C. A. Webster, R. D. MacDougall, and J. A. Rowlands, "The x-ray light valve: A low-cost digital radiographic imaging system," Med. Phys. **34**, 4609–4611 (2007).
[8]P. K. Rieppo and J. A. Rowlands, "X-ray imaging with amorphous selenium: Theoretical feasibility of the liquid crystal light valve for radiography, Med. Phys. **24**, 1279–1291 (1997).
[9]P. Oakham and J. A. Rowlands, "The optimal optical readout for the x-ray light valve—Document scanners," Med. Phys. (submitted).
[10]C. A. Webster, I. Koprinarov, and J. A. Rowlands, "The x-ray light valve: A low-cost digital radiographic imaging system—Concept and implementation," Med. Phys. **35**, 939–949 (2008).
[11]W. Que and J. A. Rowlands, "X-ray imaging using amorphous selenium: Inherent spatial resolution," Med. Phys. **22**, 365–374 (1995).
[12]H. MacMahon, C. J. Vyborny, C. E. Metz, K. Doi, V. Sabeti, and S. L. Solomon, "Digital radiography of subtle pulmonary abnormalities: An ROC study of the effect of pixel size on observer performance," Radiology **158**, 21–26 (1986).
[13]I. A. Cunningham, "Applied linear-systems theory," in *Handbook of Medical Imaging, Vol. 1. Physics and Pscychophysics*, edited by J. Beutel, H. L. Kundel, and R. L. Van Metter (SPIE, Bellingham, WA, 2000), pp. 79–159.
[14]J. T. Dobbins III, "Image quality metrics for digital systems," in *Handbook of Medical Imaging, Vol. 1. Physics and Pscychophysics*, edited by J. Beutel, H. L. Kundel, and R. L. Van Metter (SPIE, Bellingham, WA, 2000), pp. 161–222.
[15]G. Hajdok, J. Yao, J. J. Battista, and I. A. Cunningham, "Signal and noise transfer properties of photoelectric interactions in diagnostic x-ray imaging detectors," Med. Phys. **33**, 3601–3620 (2006).
[16]A. J. S. M. de Vaan, "Competing display technologies for the best image performance," J. Soc. Inf. Disp. **15**, 657–666 (2007).
[17]T. Szeto, C. A. Webster, I. Koprinarov, and J. A. Rowlands, "The x-ray light valve: A potentially low-cost, digital radiographic imaging system—A liquid crystal cell design for chest radiography," Med. Phys. **35**, 959–967 (2008).
[18]*Liquid Crystal Mixtures for Electro-Optic Displays* (Merck/BDH, Poole, UK, 1992).
[19]P. Yeh and C. Gu, *Optics of Liquid Crystal Displays* (Wiley, New York, 1999).
[20]R. M. Schaffert, *Electrophotography* (Focal, London, 1980).
[21]E. Samei, M. J. Flynn, and D. A. Reimann, "A method for measuring the presampled MTF of digital radiographic systems using an edge test device," Med. Phys. **25**, 102–113 (1998).
[22]D. M. Tucker, G. T. Barnes, and D. P. Chakraborty, "Semiempirical model for generating tungsten target x-ray spectra," Med. Phys. **18**, 211–218 (1991).
[23]L. Chowdhury, O. Tousignant, G. DeCrescenzo, P. Gauthier, J. Leboeuf, and J. A. Rowlands, "Effect of x-ray exposure on the modulation transfer function of amorphous selenium," Med. Phys. (submitted).
[24]E. Samei and M. J. Flynn, "An experimental comparison of detector performance for direct and indirect digital radiography systems," Med. Phys. **30**, 608–622 (2003).